## PROCEEDINGS OF SPIE

SPIEDigitalLibrary.org/conference-proceedings-of-spie

# Intravital hybrid optical-optoacoustic microscopy based on fiber-Bragg interferometry

Rami Shnaiderman, Georg Wissmeyer, Markus Seeger, Hector Estrada, Vasilis Ntziachristos

Rami Shnaiderman, Georg Wissmeyer, Markus Seeger, Hector Estrada, Vasilis Ntziachristos, "Intravital hybrid optical-optoacoustic microscopy based on fiber-Bragg interferometry," Proc. SPIE 10494, Photons Plus Ultrasound: Imaging and Sensing 2018,

104942M (19 February 2018); doi: 10.1117/12.2290281



Event: SPIE BiOS, 2018, San Francisco, California, United States

### Intravital hybrid optical-optoacoustic microscopy based on fiber-Bragg interferometry

Rami Shnaiderman\*ab†, Georg Wissmeyerab†, Markus Seegerab, Hector Estradab, Vasilis Ntziachristosab

<sup>a</sup>Institute of Biological and Medical Imaging (IBMI), Helmholtz Zentrum München, Neuherberg 85764, Germany; <sup>b</sup>Chair for Biological Imaging, Technische Universität München (TUM), Munich 81675, Germany

#### **ABSTRACT**

Optoacoustic microscopy (OAM) has enabled high-resolution, label-free imaging of tissues at depths not achievable with purely optical microscopy. However, widespread implementation of OAM into existing epi-illumination microscopy setups is often constrained by the performance and size of the commonly used piezoelectric ultrasound detectors. In this work, we introduce a novel acoustic detector based on a  $\pi$ -phase-shifted fiber Bragg grating ( $\pi$ -FBG) interferometer embedded inside an ellipsoidal acoustic cavity. The cavity enables seamless integration of epi-illumination OAM into existing microscopy setups by decoupling the acoustic and optical paths between the microscope objective and the sample. The cavity also acts as an acoustic condenser, boosting the sensitivity of the  $\pi$ -FBG and enabling cost effective CW-laser interrogation technique. We characterize the sensor's sensitivity and bandwidth and demonstrate hybrid OAM and second-harmonic imaging of phantoms and mouse tissue *in vivo*.

**Keywords:** Medical and biological imaging; optoacoustic microscopy; nonlinear microscopy; fiber detectors; fiber Bragg- Grating.

#### 1. INTRODUCTION

Hybrid optical and optoacoustic (O2A) microscopy enables new opportunities for biological interrogation by combining fluorescence, absorption and non-linear absorption contrast in one imaging modality <sup>1</sup>. Hybrid optical-optoacoustic setups have recently enabled simultaneous and label-free multi-contrast imaging in biological specimen <sup>2-5</sup>. However, O2A microscopy requires the combination of a microscope objective and at least one acoustic detection element placed in close proximity to the imaged specimen. Since the size of optical objectives and highly sensitive ultrasound transducers is much larger compared to the volume sampled during imaging, O2A implementations have been typically performed in transmission-mode <sup>6</sup>, i.e. by placing the specimen between the optical system and an ultrasound transducer, limiting the application of the technique mostly to *ex vivo* observations.

Epi-illumination (reflection) O2A imaging requires miniaturization of the acoustic detection elements, without hindering their performances. The optical resolutions offered by the O2A systems results in imaging of voxels with sizes of few microns up to tens of microns in each dimension. Such small voxels emit ultrasonic signals with frequencies of tens of MHz and amplitudes smaller than 100Pa <sup>7</sup>. Yet, widespread piezoelectric based transducers cannot be effectively miniaturized as the sensitivity of a piezoelectric element is proportional to the size of the active surface, therefore miniaturization leads to a quadratic decline of the detection sensitivity. The dependence of the central frequency on the thickness-resonance of the piezoelectric element imposes further constrains onto the detection bandwidth in miniaturized designs.

Photons Plus Ultrasound: Imaging and Sensing 2018, edited by Alexander A. Oraevsky, Lihong V. Wang, Proc. of SPIE Vol. 10494, 104942M · © 2018 SPIE · CCC code: 1605-7422/18/\$18 · doi: 10.1117/12.2290281

<sup>\*</sup> rami.shnaiderman@tum.de

<sup>&</sup>lt;sup>†</sup> These authors contributed equally to this work

For example, miniaturized piezoelectric elements manufactured for intravascular ultrasound detectors (IVUS) have a 1.2 mm diameter sensing area with a noise equivalent pressure (NEP) of 1.8 kPa over a 16 MHz bandwidth <sup>8</sup>, which greatly limits the sensitivity of a potential optoacoustic microscopy application.

Alternatively,  $\pi$ -phase-shifted fiber Bragg grating ( $\pi$ -FBG) interferometry can enable highly sensitive miniaturized ultrasound detection. We have recently demonstrated  $\pi$ -FBG-based optoacoustic microscopy in transmission-mode  $^9$ , achieving a NEP of 100 Pa at 20 MHz and 70 MHz central frequencies, over fractional bandwidths of 100 % and 21 %, respectively. This favorable performance employed coherence restored pulse interferometry (CRPI) for interrogating the interferometer, however the cost of CRPI is prohibitive for widespread application  $^{10}$ .

In this work, we aimed to develop a novel sensor for epi-illumination O2A microscopy addressing previous limitations. We hypothesized that we could achieve *in vivo* detection by designing a sensor that compactly locates the  $\pi$ -FBG interferometer in a close proximity to a microscope objective while effectively decoupling the acoustic and optical paths between the objective and the sample. The sensor is based on an acoustic-cavity that acts as an ultrasound condenser offering improved sensitivity alongside cost effective CW-laser interferometer interrogation technique (details regarding this technique can be found in  $^{11}$ ).

#### 2. METHODS

#### 2.1 Sensor Design

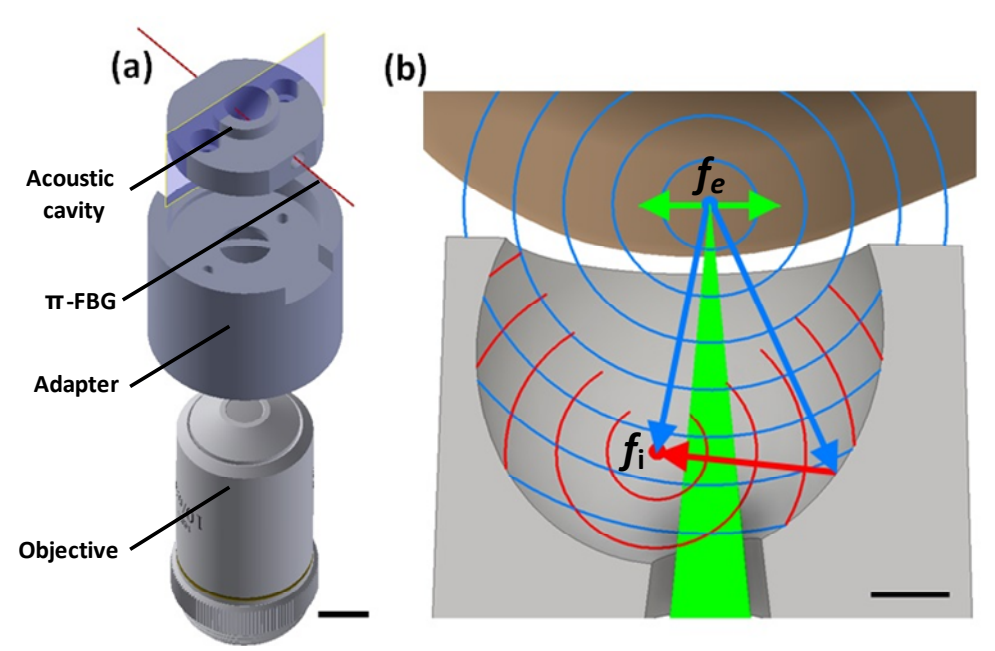
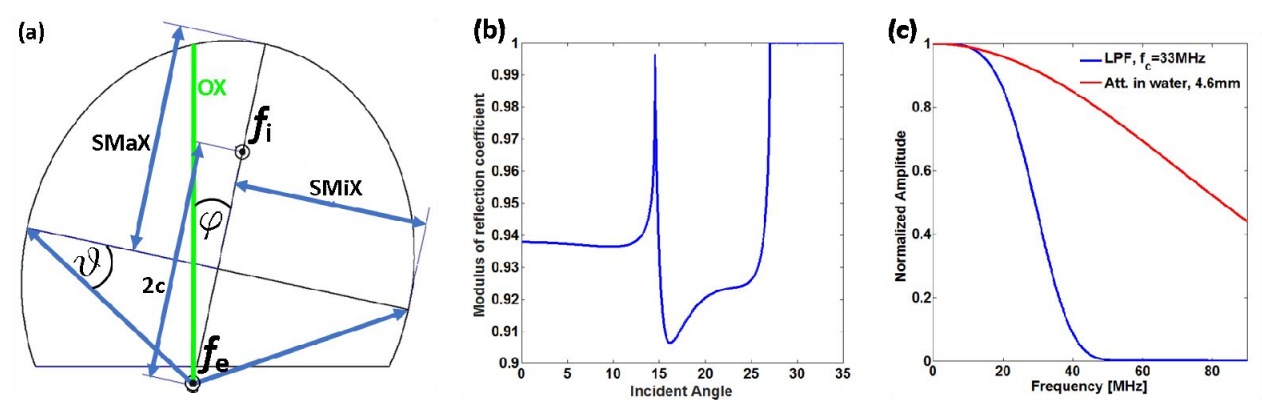


Figure 1. General outline and the operating principle of the  $\pi$ -FBG-based sensor. (a) Perspective view of components prior to assembly, showing the acoustic cavity, metal sleeve (adapter), and microscope objective. The red line indicates the position of the  $\pi$ -FBG fiber through the acoustic cavity. Scale bar, 8mm. (b) Cross-section of the acoustic cavity performed along the plane indicated in (a) illustrating the operating principle of the sensor. The laser beams for second-harmonic generation and optoacoustic excitation (green cone) enter the reflector from an aperture at the bottom and focus inside the specimen (top), the optical focus coincides with the external acoustic focus  $-f_e$ . The green arrows indicate the region of interest scanned by the excitation beams. Upon absorption, optical signals are collected by the microscope objective below the cavity (not shown); optoacoustic signals enter the acoustic cavity (blue circles), where they are reflected and focused (red circles) onto the active detection area of the  $\pi$ -FBG detector located at the inner acoustic focus of the ellipsoidal cavity  $-f_e$ . Scale bar, 1.5mm.

The sensor designed comprised of a metal sleeve, an acoustic cavity and a fiber-based  $\pi$ -FBG ultrasound detector (**Fig. 1a**), the latter is inserted into the acoustic cavity through two concentric openings on the cavity sides. The metal sleeve acted as an adaptor between the acoustic cavity and the microscope objective. **Fig. 1b** depicts the principles of operation

of the cavity. The acoustic cavity has an ellipsoidal shape, which allows for bi-focal acoustic focus: internal focal spot (denoted by " $f_e$ " in **Fig. 1b**) and an external focal spot (denoted by " $f_e$ " in **Fig. 1b**). The excitation beam enters the cavity trough an aperture at the bottom and the optical focus coincides with  $f_e$ , the generated ultrasonic signal at this point is gathered by the acoustic cavity and projected onto fi where the  $\pi$ -FBG is located. Tilting the ellipsoid on its minor axis virtually eliminates interference between the microscope's optical path and the  $\pi$ -FBG detector implementing an acoustic path that differs from the optical path between the microscope objective and the sample. The condensing effect of the cavity alongside the  $\pi$ -FBG's radial detection angle of  $360^{\circ}$  amplifies the detected signal improving the achievable single-to-noise ratio (SNR). This results in improved sensitivity toward ultrasound detection and at the same time relaxes the requirements for high sensitivity  $\pi$ -FBG interferometers and the law noise optical interrogation systems. The aperture at the bottom of the cavity was sealed using a standard circular microscope cover slip with a thickness of 170  $\mu$ m. The cavity was filled with centrifuged ultrasound gel to allow for acoustic impedance matching; then it was sealed using 10  $\mu$ m thick polyethylene foil.



**Figure 2.** Properties of the acoustic cavity. (a) Schematic of the cavity. **SMaX**, semi major axis; **SMiX**, semi minor axis; **OX**, optical axis; **c**, linear eccentricity;  $f_e$ , external acoustic focus;  $f_i$ , internal acoustic focus;  $\phi$ , tilt angle;  $\theta$ , acoustic incident angle. (b) Acoustic reflection coefficient from a steel-water interface as dependent on the incident angle. (c) Frequency dependent acoustic attenuation in the cavity and cavity imperfections modeled as a low-pass filter.

Schematic of the acoustic cavity is depicted in **Fig. 2a**. The cavity measured 4.8 mm along the semi-major axis ("SMaX" in **Fig. 2a**) and 4.1 mm along the semi-minor axis ("SMiX" in **Fig. 2a**), these dimensions were chosen to maximize the solid angle of the sensor while not exceeding the working distance of the microscope objective. The minor axis of the ellipsoid was tilted by 12° (angle " $\phi$ " in **Fig. 2a**), in relation to the optical axis ("OX" in **Fig. 2a**) of the microscope objective to clear the  $\pi$ -FBG detector from the cavity's aperture. The fi was designed to be 400  $\mu$ m outside of the rim of the cavity, this distance was chosen for an imaging depth adequate for studying mouse dermis, and it matches the depths commonly imaged by multi-photon microcopy.

The solid angle is a measure for the amount of collected acoustic signals and therefore a measure for the maximum achievable acoustic amplifude amplification of the cavity, for the dimensions presented herein the maximum amplification of 14 was estimated <sup>13</sup>. In practice, several factors limit the achievable amplification. First, the reflection coefficient of the stainless steel and water interface varies between 0.91 and 1 (**Fig. 2b**) <sup>14</sup>, corresponding to minimum and maximum incident angles of  $0^{\circ}$  and  $31.3^{\circ}$  (angle " $\theta$ " in **Fig. 2a**). Second, the propagation length in the cavity of 4.6mm induces additional frequency dependent attenuation on the ultrasonic signals (**Fig. 2c**)<sup>15</sup>. And third, misalignments and surface imperfections due to limitations in manufacturing quality interfere with the coherent summation of high-frequency waves, the global effect resembles a low-pass filter (LPF) with a cut-off frequency of 33MHz (**Fig. 2c**), see section **3.1** for more information.

#### 2.2 O2A Epi-illumination

The O2A microscope setup is illustrated schematically in **Fig. 3**. The top left image shows the sensor mounted onto an objective before the mouse holder was placed on top of the microscope translational stages. The two laser excitation beams were attenuated using a set of neutral density filters in order to adjust for different specimens, and then directed through a telescope and high-speed xy- galvanometric mirrors (6215H, Cambridge Technology, Bedford, MA, USA). In order to focus to a diffraction-limited spot, the combined beam was then enlarged to fill the back aperture of a 10x

objective lens (PLN 10X, Olympus, Hamburg, Germany; NA 0.25, working distance (WD) 10.6 mm) that was mounted on an inverted microscope (AxioObserver.D1, Carl Zeiss, Jena, Germany). The beam was then raster-scanned across a 630 µm× 630 µm field of view (FOV) during specimen imaging. Specimens were aligned to the detector using a xyzmotorized microscopy stage (xy-stage, MLS203-2, Thorlabs, Newton, NJ, USA; z-stage, ZMZS500-E, Thorlabs; step size 0.1 µm). A 3D-printed platform was attached to the xyz stage using an inlay of thin polyethylene foil. This platform allowed the immobilization of samples ranging from micrometer-sized phantoms to living mice, together with the necessary anesthesia equipment. A drop of centrifuged ultrasound gel was placed between the platform and sensor to allow transmission of acoustic signals. Second-harmonic generation (SHG) microscopy was carried out using an Ybbased, 1043 nm laser (YBIX, Time-Bandwidth, Zürich, Switzerland) with a pulse width of 170 fs; average output power, 2.8 W; and repetition rate, 84.4 MHz. The nonlinear optical emission was collected through the objective lens in backward direction mode. The signal was split from the excitation wave- length using a dichroic mirror installed in an electrical filter wheel (CDFW5, Thorlabs). Then the signal was bandpass-filtered and recorded by a photomultiplier tube (PMT H9305-03, Hamamatsu Photonics, Hamamatsu, Japan). Optoacoustic microscopy was performed using a 532 nm solid-state laser pumped by a pulsed diode (SPOT-10-100- 532, Elforlight Ltd, Daventry, UK). The repetition rate was 0-50 kHz; energy per pulse, 20 μJ; pulse width, <1.4 ns; and M<1.1. The laser pulses were detected using a photodiode (DET36A, Thorlabs), which triggered the galvanometric mirrors as well as signal acquisition. The ultrasound sensor was mounted on top of the microscope objective using an adapter plate (Fig. 1a).

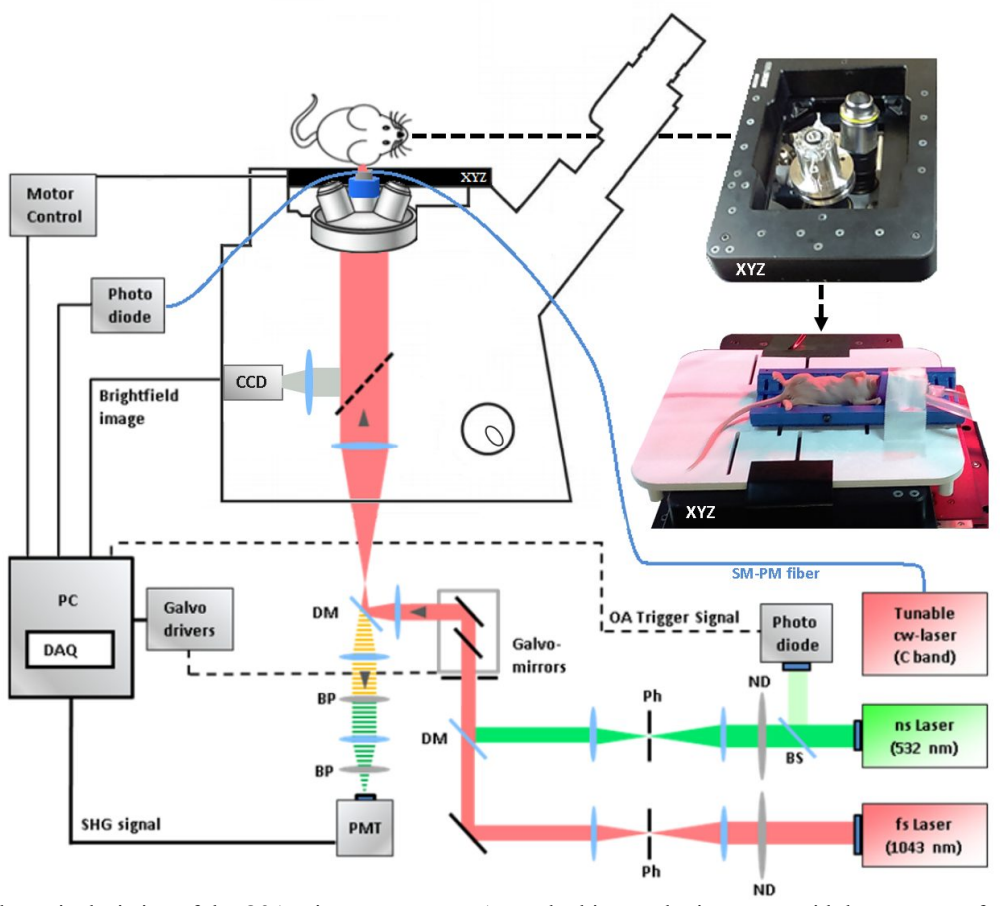


**Figure 3**. Schematic depiction of the O2A microscopy setup: A standard inverted microscope with laser sources for optoacoustic and non-linear optical imaging is combined with galvanometric mirrors for fast laser raster scanning. The sensor is mounted on the microscope objective, with a tunable CW laser coupled to the embedded  $\pi$ -FBG. The inset shows the 3D printed platform supporting an anesthetized mouse and mounted on a xyz positioning stage. **DM**, dichroic mirror; **BP**, bandpass filter; **PH**, pinhole; **ND**, neutral density filter; **BS**, beam splitter; **PMT**, photomultiplier tube; **OA**, opto- acoustic; **DAQ**, data acquisition card.

The  $\pi$ -FBG was interrogated using a tunable CW-laser (INTUN TL1550-B, Thorlabs; 1520–1630 nm, 20 mW). Transmitted light was directed to a high-bandwidth photodiode (PDB450C, Thorlabs; detection bandwidth, 150 MHz), which detected changes in the transmitted intensity. This signal was recorded using a high-speed 12-bit data acquisition (DAQ) card (ADQ412, SP Devices, Linköping, Sweden), which allowed streaming-like acquisition and therefore high-speed raster scanning of the FOV.

The FOV (maximum,  $630 \,\mu\text{m} \times 630 \,\mu\text{m}$ ) was raster-scanned by the laser excitation beams for optoacoustic and optical modalities using galvanometric mirrors controlled by a 16-bit DAQ card (PCIe 6363, National Instruments, Austin, Texas, USA) with a maximum sampling rate of 900 MS/s per channel. Resolution and step size were adjustable. After each scan, specimens were moved by the xyz stage to align the next area with the beams in order to allow stitching of larger images. The repetition rate of the optoacoustic microscopy excitation laser was 25 kHz, and the detected signals were bandpass-filtered (5–90 MHz).

#### 3. RESULTS

#### 3.1 Sensor characterization

Analyzing the ultrasonic signal recorded from a point on a polystyrene suture (19  $\mu$ m – diameter) reveals two contributions separated by ~3ms. The first signal (" $S_d$ ", **Fig. 4a**) arrived directly at the  $\pi$ -FBG and the second signal (" $S_i$ ", **Fig. 4a**) arrives indirectly after being reflected from the acoustic cavity's surface (**Fig. 1b**). An SNR analysis shows 5-fold improvement when using the indirect signal for image formation. Frequency analysis (**Fig. 2b**) shows slight attenuation of high frequencies and strong amplification of lower frequencies in the indirect signal compared to the direct. This behavior can be modeled by applying frequency dependent attenuation and LPF, mimicking the cavity's imperfections (**Fig. 2c**), onto the spectrum of the direct signal. **Fig. 4b** presents the result which is in a good agreement with the spectrum of the indirect signal.

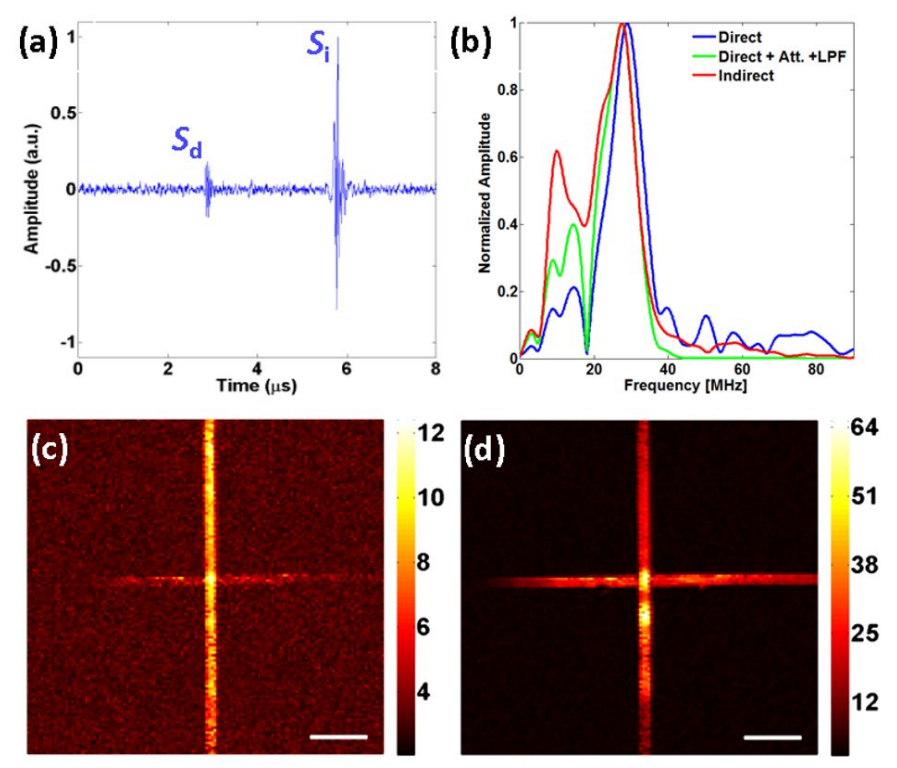


**Figure 4**. Characterization of the sensor using (a)–(d) polystyrene. (a) Optoacoustic signals from a polystyrene suture in the time domain, showing a recording of the direct signal -  $S_d$  and the indirect signal -  $S_i$  reflected and amplified by the acoustic cavity. (b) Corresponding frequency response of the sensor for direct signal (blue) and indirect signal (red). Effects of frequency dependent attenuation and the LPF modeling the cavity imperfections simulated on the spectrum of the direct signal

Imaging of a suture cross phantom was performed with a FOV of  $630x630 \mu m^2$  and resolution of 130X130 pixels. A total of 30 signals were averaged, corresponding to an acquisition time of 20 s. A typical SNR of the indirect signal was 39.8 for 30 averages, corresponding to SNR of 7.3 without averaging. **Fig. 4c** and **Fig. 4d** show the maximum intensity projections (MIP) of a suture-cross phantom, using the signals directly detected by the  $\pi$ -FBG and the reflected signals focused onto the  $\pi$ -FBG, respectively. A clear improvement in contrast is visible. In particular, the sutures in **Fig. 4d** are visible over the entire FOV, suggesting a detection angle of at least 76.5°, enabling imaging of large FOV without the need to physically move the detector.

#### 3.2 Phantom and ex vivo imaging

The O2A system with the sensor mounted was used to image phantoms and *ex vivo* samples. When using the indirect signal for image formation striking improvement to image contrast is made and invisible before details are revealed. **Fig. 5a** and **Fig. 5b** show the MIP of a polystyrene sphere ( $10 \mu m - diameter$ ) using the direct and the indirect signals respectively. The imaging was performed without averaging over a FOV of  $20X20 \mu m^2$  with a resolution of  $20X20 \mu m^2$  signals respectively. The imaging was performed without averaging over a FOV of  $500X500 \mu m^2$  with a resolution of  $50X50 \mu m^2$  pixels.

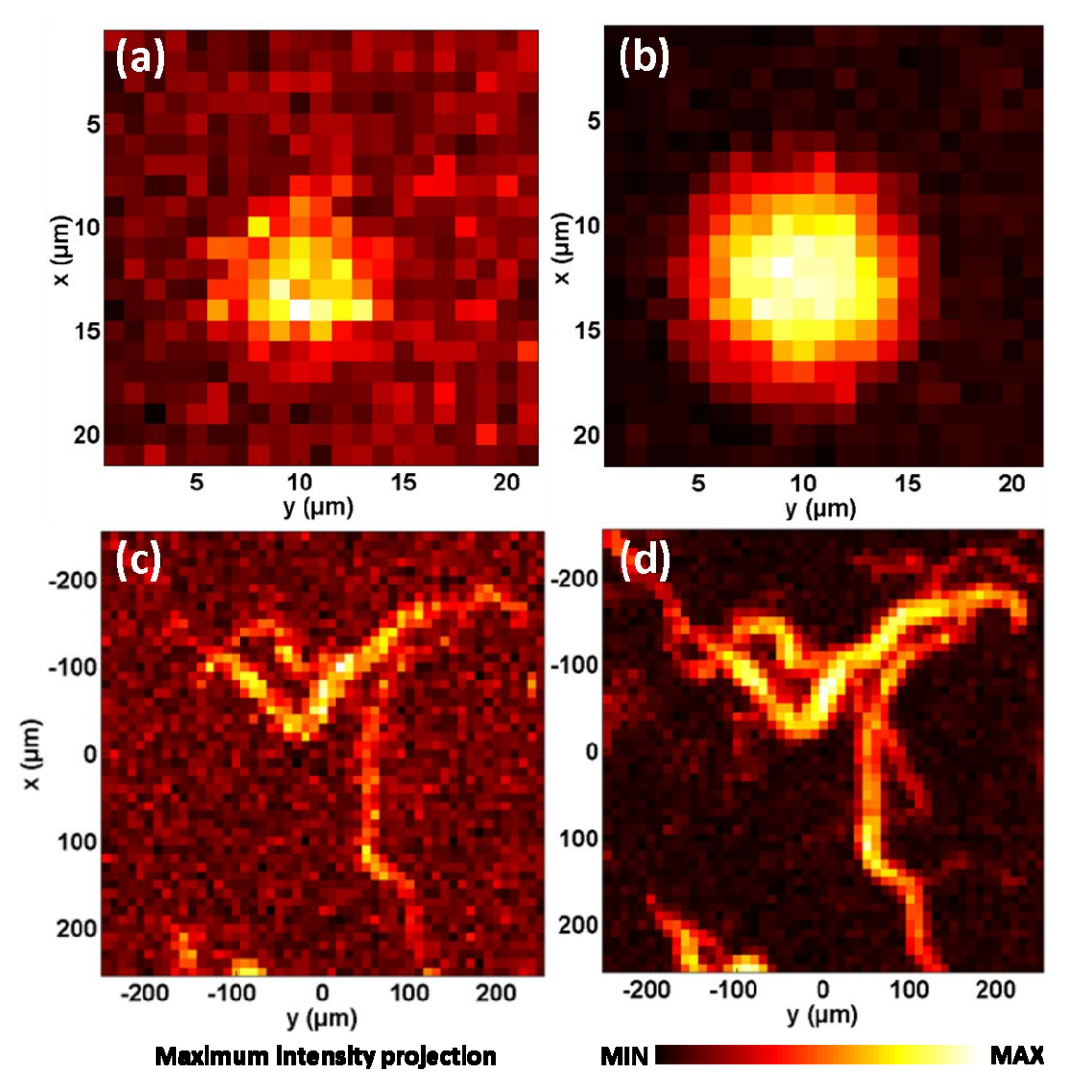


**Figure 5**. Epi-illumination O2A imaging of phantom and *ex vivo* samples. (a) MIP of a 10 μm polystyrene sphere using the direct signal. (a) MIP of a 10 μm polystyrene sphere using the indirect signal. (c) MIP of a cauterized mouse ear using the direct signal. (d) MIP of a cauterized mouse ear using the indirect signal.

#### 3.3 In vivo imaging of mouse abdomen

Next, we used our sensor to perform O2A intravital imaging of areas of the abdomen of living mice. This task can only be performed in epi-illumination, as the sample is too thick to be imaged by transmission O2A microscopes. The imaging was performed on a female Nude-1 Foxn1 mouse aged 10–12 weeks (Harlan Laboratories, Germany). The mouse was anesthetized using 1.8% isoflurane and laid onto the imaging window of the 3D-printed platform mounted atop the xyz stage. The animal experiments were approved by the government of Upper Bavaria. During *in vivo* imaging and when scanning at minimal depths of around 50 μm, laser fluence did not exceed 15 mJ/cm2. This is well below the ANSI limit of 20 mJ/cm2 for maximal permitted visible-light laser fluence on the surface of human skin <sup>16</sup>. **Fig. 6a** shows an optoacoustic image of an area of the abdomen of living mice with a FOV of 630x630 μm² and pixel size of 2.4 μm. SHG images (**Fig. 6b**) were obtained over the same region as in **Fig. 6a**. Bulges at the epidermis are visible in addition to well-defined collagen structures. The combination of the optoacoustic and SHG images (**Fig. 6c**) reveals colocalization of the complementary contrast.

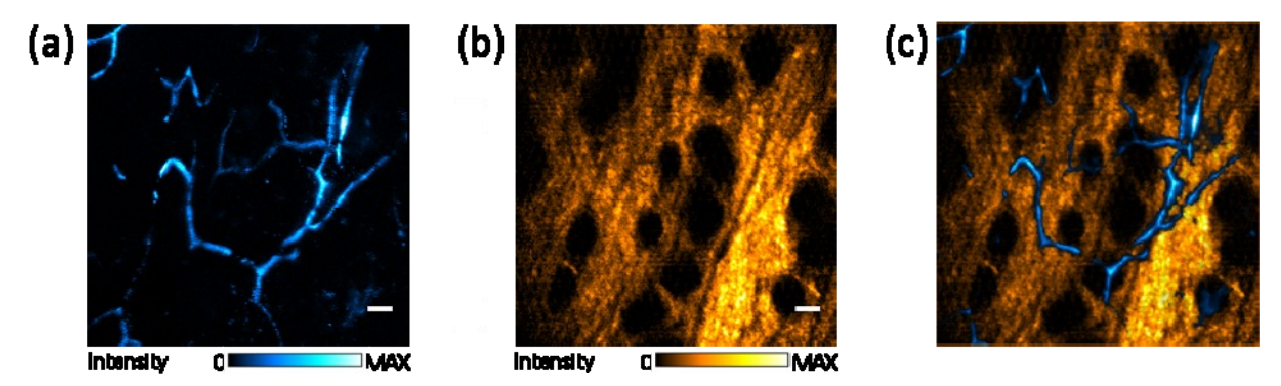


**Figure 6**. Optoacoustic microscopy and second-harmonic generation microscopy of a mouse lower rear abdomen in vivo. (a) Optoacoustic image. MIP using the indirect signal. (b) Second harmonic generation image of the same area as in (a). (c) Hybrid image of (a) and (b), indicating complementary contrast.

#### 4. DISCUSSION

In this work, we demonstrated epi-illumination hybrid optical and optoacoustic microscopy enabling intravital imaging of non-thin tissues. This capacity was enabled by a unique sensor that integrated a bi-focal acoustic cavity, a  $\pi$ -FBG interferometric detector and a simple cost-effective CW interrogation method, demonstrating a large FOV of 630X630  $\mu$ m<sup>2</sup> and being virtually invisible to the optical path. The implementation proposes a new concept for optical microscopy, by offering seamless integration of an OAM modality around conventional microscope objectives. The acoustic cavity demonstrated in this work improves the SNR of the  $\pi$ -FBG interferometer by 5-fold even when interrogated by a moderate -linewidth CW-laser. The sensitivity of  $\pi$ -FBG interferometer is directly proportional to the Q-factor of its optical cavity, by combining it with the acoustic cavity a boost to the  $\pi$ -FBG's sensitivity can be made even if a moderate Q-factor interferometer is implemented. The NEP of our sensor (88 Pa) was lower than that of a sensor interrogated by CPRI (100 Pa), even though our Q-factor was 6-fold smaller (1.9 × 10<sup>5</sup> versus 1.14 × 10<sup>6</sup>) <sup>10</sup>.

The optoacoustic integration in intravital setups can lead to next-generation optical microscopy, whereby multi-mode label- free detection of absorption contrast (optoacoustic) can be combined with optical readings to increase the information of the imaging session. Optoacoustic contrast reveals structural and functional variations in microvasculature associated with the diameters and density of blood vessels, and can enhance the information available to studies of hypertension, obesity, diabetes, inflammation, or angiogenesis <sup>17–19</sup>

The sensitivity of the sensor presented can be further improved by embedding the Bragg grating onto thin-clad or polymer fibers with lower Young modulus <sup>20</sup>, and by acoustically matching the fiber coating and medium inside the cavity.

Rami Shnaiderman acknowledges the support from the German Research Foundation (DFG) Research grant (RO 4268/4-1, CRC 1123 (Z1)).

#### 5. REFERENCES

- [1] Yao, J., and Wang, L. V, "Photoacoustic Microscopy," Laser Photon Rev 7(5), 1–36 (2014).
- [2] Tserevelakis, G.J., Soliman, D., Omar, M., and Ntziachristos, V., "Hybrid multiphoton and optoacoustic microscope," Optics Letters 39(7), 1819–1822 (2014).
- [3] Rao, B., Soto, F., Kerschensteiner, D., and Wang, L. V, "Integrated photoacoustic, confocal, and two-photon microscope.," Journal of Biomedical Optics 19(3), 36002 (2014).
- [4] Soliman, D., Tserevelakis, G.J., Omar, M., and Ntziachristos, V., "Combining microscopy with mesoscopy using optical and optoacoustic label-free modes," Scientific Reports 5(August), 12902 (2015).
- [5] Seeger, M., Karlas, A., Soliman, D., Pelisek, J., and Ntziachristos, V., "Multimodal optoacoustic and multiphoton microscopy of human carotid atheroma," Photoacoustics in press, (2016).
- [6] Strohm, E.M., Moore, M.J., and Kolios, M.C., "Single Cell Photoacoustic Microscopy: A Review," IEEE Journal of Selected Topics in Quantum Electronics 22(3), 1–15 (2016).
- [7] Wang, L. V, and Yao, J., "A practical guide to photoacoustic tomography in the life sciences," Nature methods 13(8), 627–638 (2016).
- [8] Rosenthal, A., Kellnberger, S., Bozhko, D., Chekkoury, A., Omar, M., Razansky, D., and Ntziachristos, V., "Sensitive interferometric detection of ultrasound for minimally invasive clinical imaging applications," Laser Photonics Reviews 8(3), 450–457 (2014).
- [9] Wissmeyer, G., Soliman, D., Shnaiderman, R., Rosenthal, A., and Ntziachristos, V., "All-optical optoacoustic microscope based on wideband pulse interferometry," Optics Letters 41(9), 1953 (2016).
- [10] Rosenthal, A., Razansky, D., and Ntziachristos, V., "Wideband optical sensing using pulse interferometry.," Optics express 20(17), 19016–29 (2012).
- [11] Rosenthal, A., Razansky, D., and Ntziachristos, V., "High-sensitivity compact ultrasonic detector based on a piphase-shifted fiber Bragg grating," Optics Letters 36(10), 1833–1835 (2011).
- [12] Rosenthal, A., Ángel, M., Caballero, A., and Kellnberger, S., "Spatial characterization of the response of a silica optical fiber to wideband ultrasound," Opt. Lett. 37(15), 3174–3176 (2012).
- [13] Shnaiderman, R.A.M.I., WIssmeyer, G.E., Eeger, M.A.S., Oliman, D.O.S., Strada, H.E.E., Azansky, D.A.R., Osenthal, A.M.I.R.R., and Tziachristos, V.A.N., "Fiber interferometer for hybrid optical and optoacoustic intravital microscopy," Optica 4(10), (2017).
- [14] Maey, R.G., "Acoustic microscopy: Fundamentals and applications.," John Wiley & Sons (2008).
- [15] Cheeke, J.D.N., "Fundamentals and Applications of Ultrasonic Waves," CRC Press (2002).
- [16] Wang, L. V, [Photoacoustic Imaging and Spectroscopy], CRC Press (2009).
- [17] Omar, M., Schwarz, M., Soliman, D., Symvoulidis, P., and Ntziachristos, V., "Pushing the optical imaging limits of cancer with multi-frequency-band raster-scan optoacoustic mesoscopy (RSOM)," Neoplasia (New York, N.Y.) 17(2), 208–214 (2015).
- [18] Brissova, M., Shostak, A., Fligner, C.L., Revetta, F.L., Washington, M.K., Powers, A.C., and Hull, R.L., "Human Islets Have Fewer Blood Vessels than Mouse Islets and the Density of Islet Vascular Structures Is Increased in Type 2 Diabetes," Journal of Histochemistry and Cytochemistry 63(8), 637–645 (2015).
- [19] Chao, C.Y.L., Zheng, Y.-P., and Cheing, G.L.Y., "The Association Between Skin Blood Flow and Edema on Epidermal Thickness in the Diabetic Foot," Diabetes Technology & Therapeutics 14(7), 602–609 (2012).
- [20] Gren, H., Berer, T., Felbermayer, K., Nuster, R., Paltauf, G., and Burgholzer, P., "Polymer fiber detectors for photoacoustic imaging," Proc. SPIE 7564, 75640M–75640M–5 (2010).